*Int. J. Electrochem. Sci.*, 12 **(2017)** 10187 – 10198, doi: 10.20964/2017.11.61

**International Journal of ELECTROCHEMICAL SCIENCE**
www.electrochemsci.org

# Investigation of Carbon Supported Ru–Pt Nanoparticles for High–Performance Electrocatalytic Oxidation of Methanol

*Long Quan Dang*[1,2], *Manh Tuan Nguyen*[3,4], *Nguyen Van Truong*[5], *Phuoc Huu Le*[6,*], *Nguyen Viet Long*[7,8]

[1] Department of Physics, College of Natural Sciences, Can Tho University, Campus II, 3/2 Street, Ninh Kieu District, Can Tho City, Vietnam
[2] Institute for Nanotechnology (INT), Vietnam National University - Ho Chi Minh City (VNU-HCM), Community 6, Linh Trung Ward, Thu Duc District, Ho Chi Minh City, Vietnam.
[3] Institute of Applied Materials Science, Vietnam Academy of Science and Technology, 01 Mac Dinh Chi Street, District 1, Ho Chi Minh City, Vietnam
[4] Graduate University of Science and Technology, Vietnam Academy of Science and Technology, 18 Hoang Quoc Viet Street, Cau Giay District, Ha Noi, Vietnam
[5] Faculty of fundamental sciences, Thai Nguyen University of Technology, Thai Nguyen, Vietnam
[6] Faculty of Basic Sciences, Can Tho University of Medicine and Pharmacy, 179 Nguyen Van Cu Street, Can Tho city, Vietnam
[7] Ceramics and Biomaterials Research Group, Ton Duc Thang University, Ho Chi Minh City, Vietnam
[8] Faculty of Applied Sciences, Ton Duc Thang University, Ho Chi Minh City, Vietnam
[*]E-mail: lhuuphuoc@ctump.edu.vn

*Received:* 3 August 2017 / *Accepted:* 12 September 2017 / *Published:* 12 October 2017

Platinum-nanoparticle-based catalysts are fascinating and widely used in fuel cells. This study is an attempt to develop low-cost and high performance of carbon supported Ru-Pt nanoparticles (NPs) for direct methanol fuel cells (DMFCs). We have synthesized RuPt/C, Ru@Pt/C, RuPt/MWCNT, and Ru@Pt/MWCNT nanomaterials by a facile two-step reduction method. X-ray diffraction (XRD) shows the f.c.c. Pt and h.c.p. Ru phases and the NPs are under a slight compressed strains. The synthesized NPs obtained small mean sizes ($d_{mean} \leq 3.9$ nm) and narrow size distributions (1 – 9 nm). STEM-EDS line scan profiles reveal that architecture of Ru@Pt NPs composes of Ru-core and Pt-rich–Ru alloy shell, while that of RuPt alloy NPs exhibits random arrangement of Ru and Pt atoms. The Ru@Pt/MWCNT possessed the highest methanol oxidation activity with current density ($J_f$) of 182.4 mA.cm$^{-2}$ and the lowest electron transfer resistance ($R_{et}$) of 606 Ω as compared with the other samples. The outstanding performance of Ru@Pt/MWCNT could be attributed to the high Pt dispersion, the strong synergetic effect of the Ru@Pt NPs (i.e. improving CO poisoning tolerance and enhancing the intrinsic activity of Pt), and the high porosity and electrical conductivity of MWCNT support.

**Keywords:** Electrocatalysts, Ru@Pt nanoparticles, carbon support, methanol oxidation, cyclic voltammetry.

## 1. INTRODUCTION

Direct methanol fuel cells (DMFCs) that use liquid methanol as a fuel to generate electricity are possible power sources for broad applications in both electric vehicles and portable electronics [1–3]. DMFCs offers many advantages such as low operation temperature (below 100°C), operational safety, superior specific energy and durability [3,4]. However, it remains obstacles to develop DMFCs for commercial products and applications, primarily due to the poor kinetics of methanol oxidation reactions in the anode [5]. In DMFCs, platinum (Pt) or Pt-based alloy NPs are generally used as an anode catalyst for the methanol oxidation reaction (MOR) [6–15]. Although Pt is an excellent catalyst for DMFCs, it is expensive and easy to be poisoned by carbon monoxide (CO). CO, a reaction intermediate produced during methanol oxidation, adsorbed on Pt active sites can be oxidized by $OH_{ads}$ formed on neighbouring Pt site by the following equation [10,16]:

$$CO_{ads} + OH_{ads} \rightarrow CO_2 + H^+ + e^- \quad (1)$$

An approach to improve CO tolerance and thereby enhance methanol oxidation activity is development of bimetallic heterogeneous catalysts [13–21]. It is because the presence of second metal provides –OH groups that oxidize the CO adsorbed at the neighbouring Pt sites and thus improve CO tolerance [10,22]. Recently, the preferential CO oxidation were discovered in hydrogen feeds on Ru@Pt NPs as compared with that of Ru–Pt nano-alloys [17] and of Pt shells with other metal core [22]. These findings suggest that the particle architecture is a critical factor to promote CO tolerance of Pt surface for enhancing methanol oxidation activity. An efficient way to achieve better utilization of Pt-based NPs is to disperse them onto a suitable supporting material, and thus the support it is another important factor for MOR. The support should need to have a high surface area and strong affinity, a high electrical conductivity, and an excellent chemical stability [7]. Therefore, it is essential to optimize simultaneously both the architecture of catalyst NPs and the support for achieving high-performance electrocatalytic oxidation of methanol.

In order to gain insight into the influences of the bimetallic nanoparticle architectures and the support on methanol oxidation activity, this work studied on several kinds of carbon–supported Ru–Pt NPs, namely RuPt/C, Ru@Pt/C, RuPt/MWCNT, and Ru@Pt/MWCNT. These fuel cell catalysts were selected as the studying materials because of their excellent properties for DMFCs [6–15,23–28]. A facile two-step reduction method was employed to synthesize either RuPt alloy or Ru@Pt core-shell NPs loading on Vulcan carbon (C) or multiwalled carbon nanotube (MWCNT) supports. The structural, morphological, compositional and electrochemical properties of the samples are studied and reported in detailed. This study will shed light on material selectivity, the influence factors and mechanisms for high electrocatalytic activity toward methanol oxidation.

## 2. EXPERIMENTAL DETAILS

The Ru@Pt/C and Ru@Pt/MWCNT samples with 20 wt.% Ru@Pt NPs and atomic ratio Pt:Ru = 1:1 were synthesized by using a two-step reduction method. For synthesis Ru@Pt/C samples, a mixture of 70 mg carbon black (Vulcan XC-72), 30 mL ethylene glycol (EG), and 10 mL sulfuric acid ($H_2SO_4$) was prepared in an ultrasonic bath for 15 minutes. Then, the mixture was stirred at 170°C for 30 minutes. The Ru precursor ($RuCl_3.xH_2O$ solution) was prepared by mixing 16 mg $RuCl_3.xH_2O$ with 5 mL deionized (DI) water in an ultrasonic bath for 15 min. Next, the Ru precursor was slowly dropped into the above mixture at room temperature. A solution of 200 mg $NaBH_4$ and 10 mL DI water was sprinkled into the mixture. The pH was adjusted to 12 by using NaOH 10 M solution. The mixture was stirred at room temperature for 8 hours. Afterwards, the mixture was added with a Pt precursor of $H_2PtCl_6.6H_2O$ which was prepared by mixing of 30 mg $H_2PtCl_6.6H_2O$ with 5 mL DI water. Next, the mixture was kept for reaction at room temperature for 8 hours. Finally, the Ru@Pt/C product was collected by filtration, washed thoroughly with deionized water, and dried at 100°C under vacuum overnight. For synthesis Ru@Pt/MWCNT, a similar synthesis procedure was applied, in which the MWCNT powder was used instead of the carbon black. The RuPt/C and RuPt/MWCNT samples were synthesized by co-reduction method, whose procedure was similar with the aforementioned procedure. Unlike the Ru@Pt core-shell nanoparticle synthesis, to obtain RuPt alloy NPs, the Ru and Pt precursors were added into the prepared mixture at the same time.

The crystalline orientations of the nanomaterials were studied via X-ray diffraction (XRD) with a $2\theta$-$\theta$ scan using Bruker D8 and Cu Kα (1.5406 Å) radiation. Structural characterization at atomic scale was performed in a JEOL JEM-ARM200F high-resolution scanning transmission electron microscope (HRTEM) and scanning transmission electron microscope (STEM) in high-angle annular dark field (HAADF) imaging modes, operated at 200 kV. Energy-dispersive spectrometry (EDS) line scans were carried out to study the elemental distribution of the NPs. Surface morphology of the samples were examined using field-emission scanning electron microscopy (SEM, JEOL JSM-6500) through plane-view images. The chemical stoichiometry of RuPt/MWCNT and Ru@Pt/MWCNT samples were characterized using X-ray photoelectron spectroscopy (XPS; ThermoVG 350) with the X-ray source (Mg Kα 1253.6 eV, 300 W). The binding energies obtained in the XPS analysis were standardized using C1s at 284.6 eV. XPS curve fitting was performed using the freeware XPSPEAK 4.1 with the Shirley background subtraction, and assuming a Gaussian–Lorentzian peak shape. To study the electrochemical behaviors of the samples, cyclic voltammetry (CV) curves were recorded using an Autolab system with a scan rate of 50 $mV.s^{-1}$ and a conventional three-electrode test cell. The electrolyte was a solution of 1.0 M $H_2SO_4$ and 2.0 M $CH_3OH$. The working electrode was made by 4 mg catalyst powder coated on a 1.0 $cm^2$ carbon paper. Electrochemical impedance spectroscopy (EIS) measurements were performed with an alternating current of ± 10 mV in the frequency range of 1 Hz – 100 kHz at a potential of 0.8 V.

## 3. RESULTS AND DISCUSSION

Figure 1(a) shows the XRD patterns of RuPt/C, Ru@Pt/C, RuPt/MWCNT, and Ru@Pt/MWCNT. It shows several diffraction peaks which could be indexed to the (111), (200), (220)

and (311) planes of a typical face-centered-cubic (f.c.c) lattice structure of platinum. The Ru and Pt components were extracted and analyzed by fitting the XRD spectra in 2θ range of 35 – 51°, as shown in Figure 1(b). The arrows indicate the positions of Pt (111) and Ru (200) peaks. As compared with Ru–Pt alloy and bulk Pt, the Pt (111) and Ru (200) peaks of the Ru@Pt core-shell structures are noticeably shifted to higher 2$\theta$ and lower 2$\theta$, respectively. These anomalies indicate that Ru core has a compressed lattice and Pt shell possesses tensile strain, which may be attributed to incomplete lattice formation and strains associated with the two-dimensional structure at Pt shells [17]. This abnormally XRD result is consistent with that of the Ru@Pt NPs in Ref. [17]. In addition, the inset in Figure 1(a) presents the *a*- and *c*-lattice constants of the samples and those of the database values. The *a*-lattice constant of the samples is slightly smaller than that of pure Pt at 3.923 Å (JCPDS 04-0802); meanwhile, the *c*-lattice constant is slightly higher than the Ru database value of 4.282 Å (JCPDS 06-0663), indicating the NPs in this study are under a slight compressed strains.

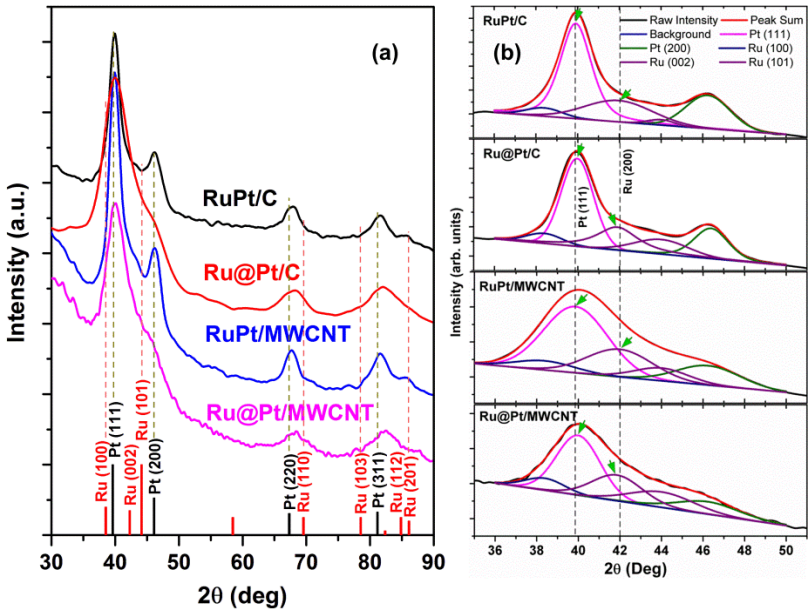


**Figure 1.** (a) XRD patterns of RuPt/C, Ru@Pt/C, RuPt/MWCNT, and Ru@Pt/MWCNT. Black vertical lines represent the f.c.c. Pt phase (JCPDS file 04-0802), and red vertical lines represent the h.c.p. Ru phase (JCPDS file 06-0663). (b) The fitting of the XRD spectra in the 2θ range of 35 – 51°, which reveals the Pt and Ru peaks. Inset in (a) presents the calculated lattice parameters of the four samples.

Figure 2 shows the typical HRTEM images of RuPt/C, Ru@Pt/C, RuPt/MWCNT, and Ru@Pt/MWCNT samples. The RuPt and Ru@Pt NPs are uniform dispersion and strong bonding with the carbon supports. As shown in the insets of Figures 2(a,c,d), the NPs exhibit the lattice fringes with d-spacing of approximately 0.21 nm and 0.23 nm, corresponding to the (002) planes of Ru and the (111) planes of Pt, respectively. The core-shell and alloy bimetallic architectures of the NPs are confirmed by STEM-EDS line scan spectra recorded from multiple single particles (Figures 2e and 2f). The EDS line scan profiles of a typical Ru@Pt nanoparticle show a bimodal Pt distribution that

reaches a maximum at the edge of the particle (i.e. the shell), whereas the Ru line shows maximum Ru concentration at the center of the particle (Figure 2e). This elemental profile reveals a core-shell architecture for Ru@Pt particles that composes of Ru core and the Pt-rich–Ru alloy shell. In contrast, for RuPt alloy NPs, both Ru and Pt line scan profiles are single Gaussian distributions across the particle, indicating the random arrangement of Ru and Pt atoms in the bulk and on the surface of RuPt NPs (Figure 2f). Based on the STEM-EDS results, graphical representations of Ru@Pt and RuPt NP architectures are shown schematically in the insets of Figures 2(e) and 2(f).

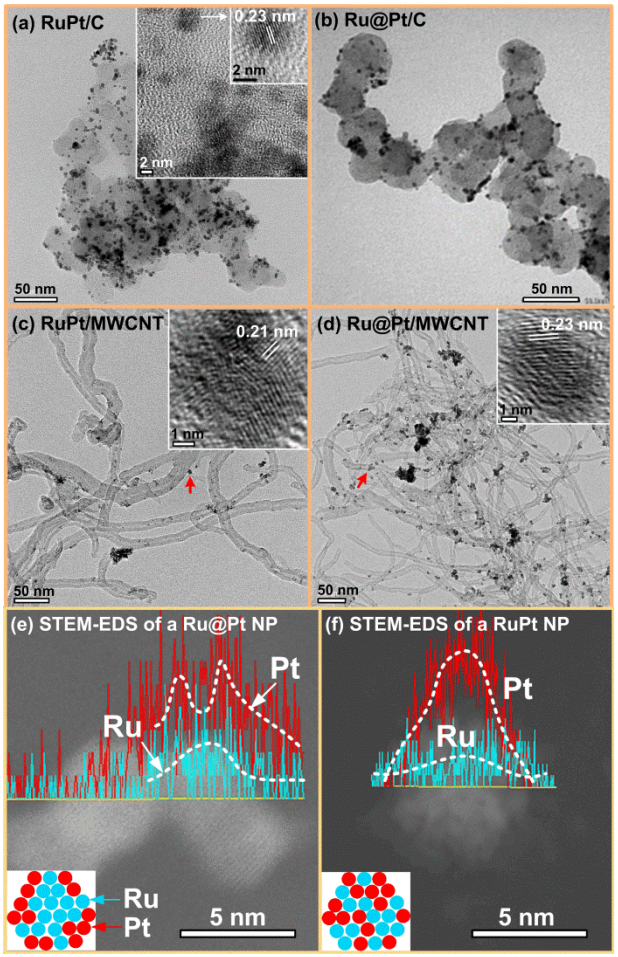


**Figure 2.** TEM images: (a) RuPt/C, (b) Ru@Pt/C, (c) RuPt/MWCNT, and (d) Ru@Pt/MWCNT. Insets in (a,c,d) show HRTEM images of a typical particle of the corresponding samples at the arrow positions. Representative STEM-EDS line spectra of (e) a ~4.5 nm Ru@Pt core-shell NP and (f) a ~7.3 nm RuPt alloy NP. The dash lines are guides to the eye. The schematic models show the architectures of Ru@Pt NP (the inset in (e)) and RuPt NP (the inset in (f)).

Figure 3 shows the structure–morphology of the samples to visualize the porosity and distribution of particles on the carbon supports [C (left) *vs.* MWCNT (right)]. MWCNT offers higher porosity and better particle dispersion – distribution than those of C support. In fact, C support shows tightly staking amongst C sheets (or agglomeration) to form as a dense material, which can limit both the particle dispersion and the specific electrochemical active area.

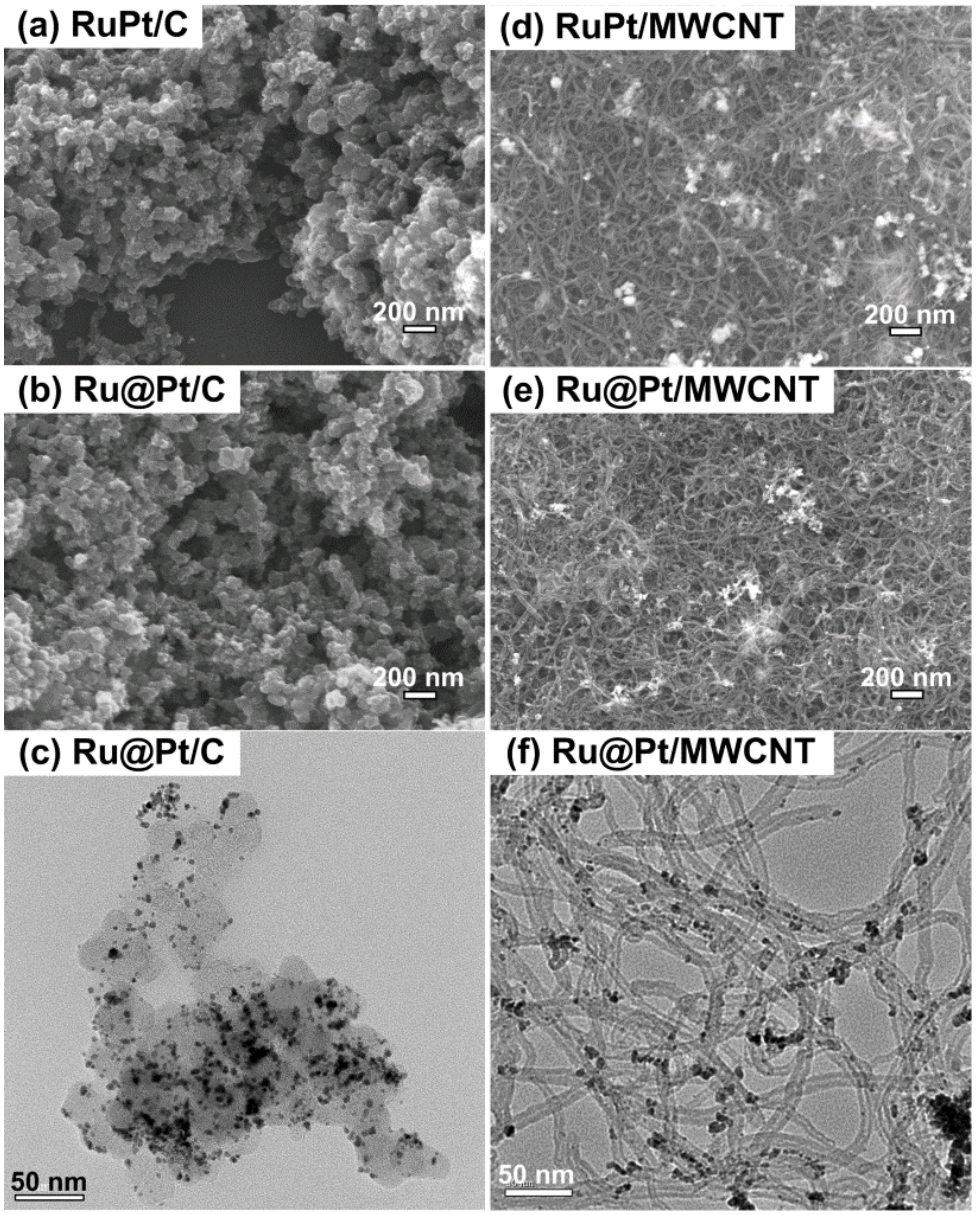


**Figure 3.** SEM and TEM images of the samples in this study.

The particle size distributions of the samples are presented in Figure 4(a–d). It exhibits narrow distributions and small mean values ($d_{mean}$). Particularly, the distribution ranges and $d_{mean}$ values are 2 – 9 nm ($d_{mean}$ = 3.9 nm) for RuPt/C, 1 – 8 nm ($d_{mean}$ = 3.4 nm) for Ru@Pt/C, 1 – 7 nm ($d_{mean}$ = 2.6 nm) for RuPt/MWCNT, and 2 – 7 nm ($d_{mean}$ = 3.5 nm) for Ru@Pt/MWCNT. By considering both $d_{mean}$ values and the upper tails of NP distributions, MWCNT support with higher porosity likely hinders the growth of the electrocatalyst NPs. This observation is consistent with the result in ref. [14], in which the mesoporous carbon support was found to restrict the crystal growth of Pt–Ru particles. The nanoparticle sizes in this study are comparable with the NP sizes of 4.1 – 4.4 nm in ref. [17] and 3.1 – 3.3 nm in ref. [5].

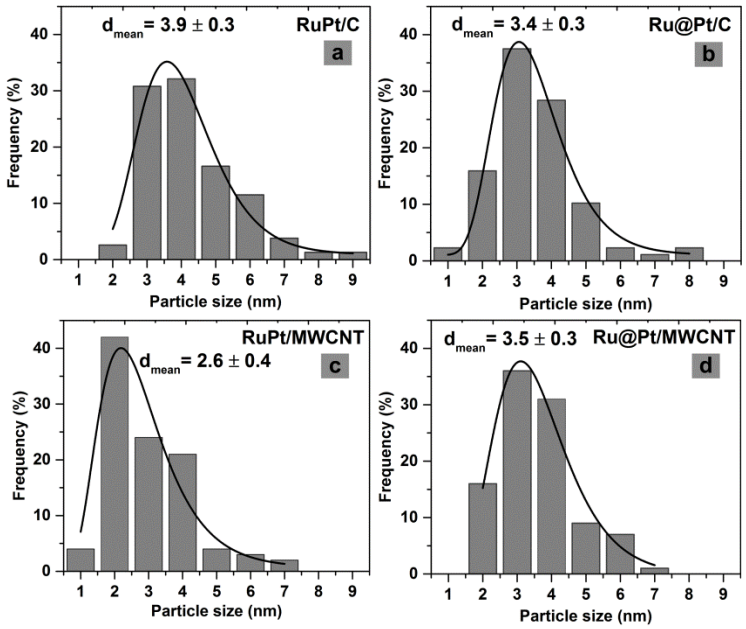


**Figure 4.** Particle size distributions of (a) RuPt/C, (b) Ru@Pt/C, (c) RuPt/MWCNT, and (d) Ru@Pt/MWCNT. Histograms are made by counting 100 particles from multiple HRTEM images taken in different sample regions. The solid lines are the log-normal fitting.

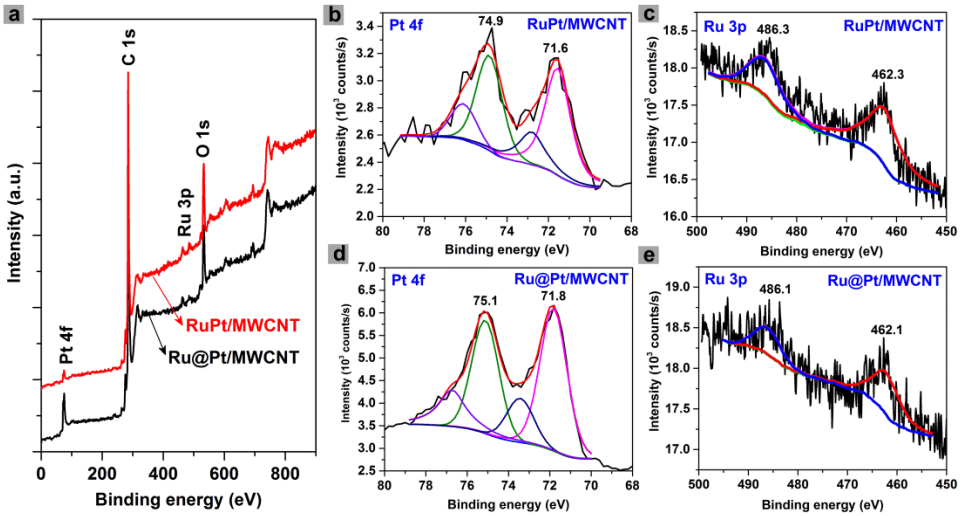


**Figure 5.** (a) Wide-scan XPS spectra of RuPt/MWCNT and Ru@Pt/MWCNT samples. High-resolution XPS spectra of (b) Pt 4f and (c) Ru 3p of the RuPt/MWCNT, (d) Pt 4f and (e) Ru 3p of the Ru@Pt/MWCNT. The black solid lines are the experimental load and the other solid lines are the fitting curves.

We performed XPS experiments on RuPt/MWCNT and Ru@Pt/MWCNT to study the surface properties and chemical states of the samples (Figure 5). The full-range scans in Figure 5(a) shows the major C, O, Pt and Ru peaks. In addition, as compared to the binding energies of pure Ru $3p_{5/2}$ (163.1 eV) and Pt $4f_{7/2}$ (71.52 eV) reported in ref. [13], the Ru $3p_{5/2}$ and Pt $4f_{7/2}$ of RuPt/MWCNT and Ru@Pt/MWCNT shifted positively and negatively by 0.8 – 1.0 eV and 0.1 – 0.3 eV, respectively. This indicates the occurrence of charge transfer from Ru to Pt (a large electronegativity metal) for forming

the RuPt alloy or Ru@Pt core-shell NPs. This XPS result is consistent with that of reported in the earlier work [13].

Figure 6 shows the cyclic voltammograms (CV) of RuPt/C, Ru@Pt/C, RuPt/MWCNT, and Ru@Pt/MWCNT in 1.0 M $H_2SO_4$ and 2.0 M $CH_3OH$ aqueous solution. The highest current densisty values of forward and reverse scans ($J_f$ and $J_r$) and $J_f/J_r$ ratio are reported in Table 1. The $J_f$ values are 24.60, 64.48, 63.32, and 182.4 mA.cm$^{-2}$ for RuPt/C, Ru@Pt/C, RuPt/MWCNT, and Ru@Pt/MWCNT, respectively. In addition, the $J_r$ values are 6.397 mA.cm$^{-2}$ for RuPt/C, 7.257 mA.cm$^{-2}$ for Ru@Pt/C, and 54.99 mA.cm$^{-2}$ for Ru@Pt/MWCNT. Noticeably, the $J_r$ peak of RuPt/MWCNT cannot be observed clearly from the CV curve (Figure 6c). The anodic peak in the reverse scan can link to the removal of the incomplete oxidized carbonaceous species, such as CO, $HCOO^-$, $HCO^-$, accumulated on the catalyst surface during the forward anodic scan [29,30]. In methanol oxidation reaction, CO is a critical intermediate that cause a lower fuel cell potential and energy conversion efficiency. Consequently, the $J_f/J_r$ ratio can be used to describe the catalyst tolerance to carbonaceous species accumulation [31]. The larger $J_f/J_r$ value regards as the better CO resistant catalyst. As summarized in Table 1, the Ru@Pt/C sample exhibited the highest $J_f/J_r$ value of 8.89, suggesting it achieved the best carbonaceous species tolerance ability amongst the samples.

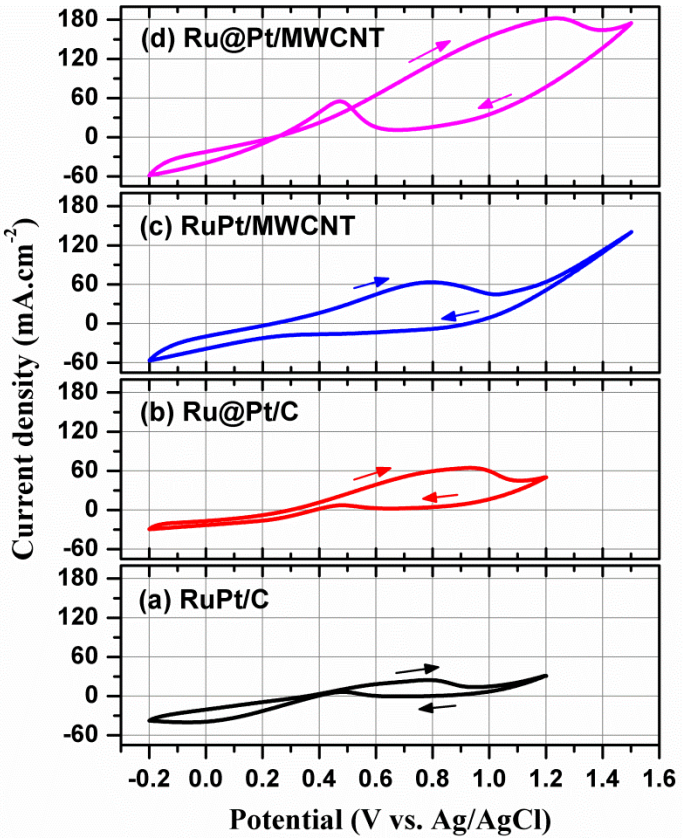


**Figure 6.** CV curves of electrocatalytic samples: (a) RuPt/C, (b) Ru@Pt/C, (c) RuPt/MWCNT, and (d) Ru@Pt/MWCNT, measured in 1.0 M $H_2SO_4$ + 2.0 M $CH_3OH$ solution with a scan rate of 50 mV.s$^{-1}$.

For the support effect, the $J_f$ of MWCNT support is always higher than that of the C support (see Figure 6 and Table 1). It can be explained that MWCNT support has higher porosity and better dispersion–distribution of the particles than the C support, as shown in Figures 2 and 3. Therefore, the MWCNT support offers higher methanol oxidation activity than C one, and this result is consistent with previous reports in the literature [15]. Regardless the supports (C or MWCNT), the core-shell NPs (i.e. Ru core and Pt-rich–Ru alloy shell, Fig. 2e inset) presents higher activity for MOR than that of RuPt alloy NPs (Figure 6). This result is in good agreement with those reported in refs. [17,20], in which the core-shell particles exhibited higher activities for preferential oxidation of CO in hydrogen than those of the alloys for both PtRu and PtRh bimetallic systems. For referencing, Table 2 summarizes the mean size of nanoparticles, measuring condition, and catalyst performance of some RuPt-based catalysts in the literature. Since the measuring condition affects the values of current density, it is hard to make a reliability comparison. Nevertheless, it can be found that a relatively high current density (i.e. 54.99 $mAcm^{-2}$) is achieved for the Ru@Pt/MWCNT in this study.

**Table 1**. Electrochemical parameters of the nanomaterials in this study.

| Sample | $J_f$ ($mA.cm^{-2}$) | $J_r$ ($mA.cm^{-2}$) | $J_f/J_r$ | $R_{et}$ (Ω) |
|---|---|---|---|---|
| RuPt/C | 24.60 | 6.397 | 3.85 | 9052 |
| Ru@Pt/C | 64.48 | 7.257 | 8.89 | 3667 |
| RuPt/MWCNT | 63.32 | - | - | 4891 |
| Ru@Pt/MWCNT | 182.4 | 54.99 | 3.32 | 606 |

**Table 2.** Mean particle size, measuring condition, and catalyst performance of some relevant RuPt-based catalysts in the literature.

| Catalyst | Mean metal particle size (nm) | Catalyst performance | | Reference |
|---|---|---|---|---|
| | | Measurement condition | Current density | |
| PtRu (1: 1)/C | 3.1 | - | - | [5] |
| PtRu (1:1)/MWCNT | 3.2 | - | - | [5] |
| PtRu (4:6) | 4.4 | - | - | [17] |
| Ru@Pt (4:6) | 4.1 | - | - | [17] |
| PtRu (1: 1)/CNTs | - | 20 mV. $s^{-1}$, 1 M $CH_3OH$ + 0.5 M $H_2SO_4$ | 34 $mA.cm^{-2}$ (loading 4 $mg.cm^{-2}$) | [15] |
| PtRu (1: 1)/C | - | 20 mV. $s^{-1}$, 1 M $CH_3OH$ + 0.5 M $H_2SO_4$ | 23 $mA.cm^{-2}$ (loading 4 $mg.cm^{-2}$) | [15] |
| RuPt (1: 1)/C | - | 10 mV. $s^{-1}$, 0.5 M 2 M $CH_3OH$ + $H_2SO_4$ | 620 μA/μg Pt | [10] |
| Ru@Pt (4: 6)/C | - | 10 mV. $s^{-1}$, 0.5 M 2 M $CH_3OH$ + $H_2SO_4$ | 680 μA/μg Pt | [10] |

Several synergistic effects could attribute to the aforementioned result (core-shell *vs.* alloy). First, Ru@Pt core-shell structure has better preferential oxidation of CO in hydrogen than that of RuPt alloy [17,20], leading to the better CO tolerance for Ru@Pt than RuPt. For the present structure of Ru-

core and Pt-rich–Ru alloy shell, Ru atoms provide –OH groups at lower potential to facilitate the oxidation of CO and poisonous intermediates adsorbed onto Pt atoms [10,16]. Second, the intrinsic activity of Pt can be enhanced because of the charge transfer from Ru to Pt, as suggested by the above XPS results and by Chen et al. [13]. Finally, in bimetallic systems, the electronic structures of the surface metals can be altered greatly by the changes in architectural configurations that facilitate alternate reaction mechanisms relative to pure Pt [20,21,32–34]. Briefly, thanks to combining the positive effects of both the nanoparticle architecture and the support factors, the Ru@Pt/MWCNT achieves the best electrocatalytic activity toward methanol oxidation.

Figure 7 shows the Nyquist plot (negative imaginary *vs.* real component of the total complex impedance Z) for all the samples at a potential of 0.8 V (*vs.* Ag/AgCl). Although the Nyquist curves of the samples do not show full semicircles, it is still clear to see that Ru@Pt/MWCNT exhibit the smallest semicircle (or the smallest resistance) as compared with the other samples. For quantitative analysis the EIS data, we employed the Randles equivalent circuit model [35], which used to fit plots with one semi-circle [36] and Pt-C-based materials [37]. The circuit included the electron transfer resistance ($R_{et}$), solution resistance ($R_s$) and double layer capacity ($C_{dl}$) of the samples (see the inset in Fig. 7). The circular fits with the Randles circuit yield $R_{et}$ values of 606, 3667, 4891, and 9052 Ω for Ru@Pt/MWCNT, Ru@Pt/C, RuPt/MWCNT, and RuPt/C, respectively. Reasonably, the lower $R_{et}$ is coincident with the higher current density at 0.8 V (Fig. 6). Both CV and EIS results demonstrate that Ru@Pt/MWCNT possesses the superior electrocatalytic activity (with the smallest $R_{et}$) over the other material systems toward methanol oxidation.

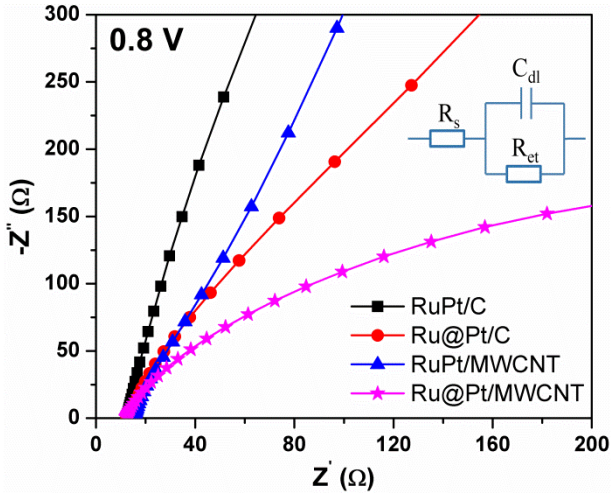


**Figure 7.** Nyquist plots of the EIS for RuPt/C, Ru@Pt/C, RuPt/MWCNT, Ru@Pt/MWCNT in a solution of 1.0 M $H_2SO_4$ containing 2.0 M $CH_3OH$, in a frequency range from 1 Hz to 100 kHz. The inset shows the Randles equivalent circuit that used to fit the EIS data.

## 4. CONCLUSION

We report the synthesis and characterization of RuPt alloy- and Ru@Pt core-shell- NPs on C and MWCNT supports for high-performance methanol oxidation. XRD and TEM results confirm the obtained RuPt and Ru@Pt NPs with averaged sizes below 4 nm. The Ru@Pt core–alloy shell NPs and

conventional RuPt alloy NPs were successfully synthesized, as indicated by STEM-EDS results. The $J_f$ ($R_{et}$) values of RuPt/C, Ru@Pt/C, RuPt/MWCNT, and Ru@Pt/MWCNT are 24.60 mA.cm$^{-2}$ (9052 Ω), 64.48 mA.cm$^{2}$ (3667 Ω), 63.32 mA.cm$^{-2}$ (4891 Ω), and 182.4 mA.cm$^{-2}$ (606 Ω), respectively. The best methanol oxidation activity of Ru@Pt/MWCNT could be attributed to the high Pt dispersion, the enhancements of CO tolerance and the intrinsic activity of Pt, and the high porosity and electrical conductivity of MWCNT support.

ACKNOWLEDGEMENTS
Financial support from Vietnam National Foundation for Science and Technology Development (NAFOSTED) under grant number 103.99–2015.17. The authors would like to thank Dr. Hong Quan Nguyen, National Chiao Tung University, Hsinchu 30049, Taiwan for helping on taking TEM images and STEM-EDS data.

## References

1. D. Bokach, J.L.G. de la Fuente, M. Tsypkin, P. Ochal, I.C. Endsjø, R. Tunold, S. Sunde and F. Seland, *Fuel Cells*, 11 (2011) 735.
2. Z. Liu, L. Hong and S.W. Tay, *Mater. Chem. Phys.*, 105 (2007) 222.
3. S. Zhao, H. Yin, L. Du, G. Yin, Z. Tang and S. Liu, *J. Mater. Chem. A*, 2 (2014) 3719.
4. X. Lu, J. Hu, J.S. Foord and Q. Wang, *J. Electroanal. Chem.*, 654 (2011) 38.
5. J. Prabhuram, T.S. Zhao, Z.K. Tang, R. Chen and Z.X. Liang, *J. Phys. Chem. B*, 110 (2006) 5245.
6. S.H. Joo, S.J. Choi, I. Oh, J. Kwak, Z. Liu, O. Terasaki and R. Ryoo, *Nature*, 412 (2001) 169.
7. R. Lv, T. Cui, M.-S. Jun, Q. Zhang, A. Cao, D.S. Su, Z. Zhang, S.-H. Yoon, J. Miyawaki, I. Mochida and F. Kang, *Adv. Funct. Mater.*, 21 (2011) 999.
8. A.S. Moura, J.L.C. Fajín, M. Mandado and M.N.D.S. Cordeiro, *Catalysts*, 7 (2017) 47.
9. M. Liu, R. Zhang and W. Chen, *Chem. Rev.*, 114 (2014) 5117.
10. N. Muthuswamy, J.L.G. de la Fuente, D.T. Tran, J. Walmsley, M. Tsypkin, S. Raaen, S. Sunde, M. Rønning and D. Chen, *Int. J. Hydrogen Energy*, 38 (2013) 16631.
11. A. Arun, M. Gowdhamamoorthi, K. Ponmani, S. Kiruthika and B. Muthukumaran, *RSC Adv.*, 5 (2015) 49643.
12. I. Ávila-García, C. Ramírez, J.M. Hallen López and E.M. Arce Estrada, *J. Alloys Compd.*, 495 (2010) 462.
13. D. Chen, Y. Li, S. Liao, D. Su, H. Song, Y. Li, L. Yang and C. Li, *Sci. Rep.*, 5 (2015) 11604.
14. J.R.C. Salgado, V.A. Paganin , E.R. Gonzalez, M.F. Montemora, I. Tacchini, A. Anson, M.A. Salvador, P. Ferreira, F.M.L. Figueiredo and M.G.S. Ferreira, *Int. J. Hydrogen Energy*, 38 (2013) 910.
15. Z. Cui, C. Liu, J. Liao and W. Xing, *Electrochimica Acta*, 53 (2008) 7807.
16. S. Jones, K. Tedsree, M. Sawangphruk, J.S. Foord, J. Fisher, D. Thompsett and S.C.E. Tsang, *ChemCatChem.*, 2 (2010) 1089.
17. S. Alayoglu, A.U. Nilekar, M. Mavrikakis and B. Eichhorn, *Nat. Mater.*, 7 (2008) 333.
18. S. Alayoglu, P. Zavalij, B. Eichhorn, Q. Wang, A.I. Frenkel and P. Chupas, *ACS Nano.*, 3 (2009) 3127.
19. Y.-C. Hsieh, Y. Zhang, D. Su, V. Volkov, R. Si, L. Wu, Y. Zhu, W. An, P. Liu, P. He, S. Ye, R.R. Adzic and J.X. Wang, *Nat. Commun.*, 4 (2013) 2466.
20. S. Alayoglu and B. Eichhorn, *J. Am. Chem. Soc.*, 130 (2008) 17479.
21. J. Greeley and M. Mavrikakis, *Nat. Mater.*, 3 (2004) 810.
22. A.U. Nilekar, S. Alayoglu, B. Eichhorn and M. Mavrikakis, *J. Am. Chem. Soc.*, 132 (2010) 7418.
23. R. Wang, H. Li, H. Feng, H. Wang and Z. Lei, *J. Power Sources*, 195 (2010) 1099.

24. Z.B. Wang, P.-J. Zuo and G.-P. Yin, *J. Alloys Compd.*, 479 (2009) 395.
25. C. Yang, D. Wang, X. Hu, C. Dai and L. Zhang, *J. Alloys Compd.*, 448 (2008) 109.
26. E. Antolini, T. Lopes and E.R. Gonzalez, *J. Alloys Compd.*, 461 (2008) 253.
27. C. Li, Z. Shao, M. Pang, C.T. Williams, X. Zhang and C. Liang, *Ind. Eng. Chem. Res.*, 51 (2012) 4934.
28. Z.B. Wang, G.P. Yin and P.F. Shi, *J. Alloys Compd.*, 420 (2006) 126.
29. R. Mancharan and J.B. Goodenough, *J. Mater. Chem.*, 2 (1992) 875.
30. S. Sun, G. Zhang, N. Gauquelin, N. Chen, J. Zhou, S. Yang, W. Chen, X. Meng, D. Geng, M.N. Banis, R. Li, S. Ye, S. Knights, G.A. Botton, T.-K. Sham and X. Sun, *Sci. Rep.*, 3 (2013) 1775.
31. Q.-L. Naidoo, S. Naidoo, L. Petrik, A. Nechaev and P. Ndungu, *Int. J. Hydrogen Energy.*, 37 (2012) 9459.
32. J. Greeley, W.P. Krekelberg and M. Mavrikakis, *Angew. Chemie - Int. Ed.*, 43 (2004) 4296.
33. J.A. Rodriguez, R.A. Campbell and D.W. Goodman, *J. Phys. Chem.*, 94 (1990) 6936.
34. J.A. Rodriguez, R.A. Campbell and D.W. Goodman, *J. Phys. Chem.*, 95 (1991) 5716.
35. J.E.B. Randles, *Discuss. Faraday Soc.*, 1 (1947) 11.
36. B. Wickman, A.B. Fanta, A. Burrows, A. Hellman, J.B. Wagner and B. Iandolo, *Sci. Rep.*, 7 (2017) 40500.
37. A.T.E. Vilian, M. Rajkumar, S.-M. Chen, C.-C. Hu, K.M. Boopathi and C.-W. Chu, *RSC Adv.*, 4 (2014) 41387.